

Analysis and Validation of High-Resolution Wind From ASCAT

Richard D. Lindsley, *Member, IEEE*, Jeffrey R. Blodgett, and David G. Long, *Fellow, IEEE*

Abstract—The standard ocean wind product from the Advanced Scatterometer (ASCAT) is retrieved on a 12.5-km grid. Ultrahigh-resolution (UHR) processing enables ASCAT wind retrieval on a high-resolution 1.25-km grid. Ideally, such a high-resolution grid allows for improved analysis of winds with high spatial variability, such as those in near-coastal regions and storms. This paper provides an analysis and validation of ASCAT UHR wind estimates to evaluate its spatial resolution and accuracy. This is done via a comparison with two other sources: buoy-measured winds in coastal regions and winds estimated from synthetic aperture radar (SAR) data over the open ocean. Near-coastal ocean measurements may be contaminated by nearby land, introducing a wind speed bias in the retrieved winds. To enable near-coastal UHR wind retrieval, we use a land contribution ratio (LCR) approach to discard ASCAT measurements with high land contamination before UHR processing and wind retrieval. Through a comparison with near-coastal buoy winds, we find that the LCR approach is appropriate for precisely controlling the tradeoff between land contamination and spatial coverage near land. We find that the resolution of the UHR data is improved over the 25-km wind product to 10 km, and likely down to 4 km in some cases. In comparing SAR and UHR winds, we find that both products have common fine-scale features and have derivative fields that match well and that the UHR product matches better the expected spectral properties of ocean winds.

Index Terms—Advanced Scatterometer (ASCAT), remote sensing, spaceborne radar, spatial resolution, wind.

I. INTRODUCTION

SCATTEROMETERS measure the radar backscatter (σ°) of the ocean surface, which is directly related to the roughness of the water from centimeter-scale waves caused by friction with ocean winds. This relationship is governed by a geophysical model function (GMF). Ground processing of σ° measurements permits inversion of the GMF to estimate the wind from the backscatter measurements [1].

Advanced Scatterometer (ASCAT) is a wind scatterometer that has been in operation since 2007. Similar to most scat-

Manuscript received November 27, 2015; revised March 19, 2016; accepted May 2, 2016. Date of publication June 7, 2016; date of current version August 11, 2016.

R. D. Lindsley was with the Microwave Earth Remote Sensing Laboratory, Brigham Young University, Provo, UT 84602 USA. He is now with Remote Sensing Systems, Santa Rosa, CA 95401 USA (e-mail: lindsley@remss.com).

J. R. Blodgett was with the Microwave Earth Remote Sensing Laboratory, Brigham Young University, Provo, UT 84602 USA. He is now with Lockheed Martin Mission Systems and Training, Manassas, VA 2010 USA (e-mail: blodgett@mers.byu.edu).

D. G. Long is with the Department of Electrical and Computer Engineering and the Microwave Earth Remote Sensing Laboratory, Brigham Young University, Provo, UT 84602 USA (e-mail: long@ee.byu.edu).

Color versions of one or more of the figures in this paper are available online at <http://ieeexplore.ieee.org>.

Digital Object Identifier 10.1109/TGRS.2016.2570245

terometers, wind vectors are retrieved at standard resolutions of 25 and 50 km, posted on 12.5- and 25-km swath grids, respectively. The standard 25-km Level-2 wind product, which is referred to in this paper as L2W, provides enough information for most applications. However, the spatial resolution may be insufficient in some applications, particularly in near-coastal regions and storms.

Higher-resolution winds may be retrieved from the same scatterometer σ° data using a method known as ultrahigh-resolution (UHR) processing. UHR processing is a limited form of image reconstruction that takes advantage of overlapping measurement footprints and provides resolution enhancement. For ASCAT, the UHR product is retrieved on a 1.25-km grid. The finer grid spacing versus L2W enables a data product with higher-frequency information, thus supporting these higher-resolution applications. However, the effective resolution of the UHR data is coarser than that suggested by the grid spacing alone due to measurement geometry and the size of the measurement footprints.

Due to the distributed nature of the ASCAT measurement footprints, σ° ocean measurements close to land may contain contributions from both land and ocean data. Such measurements are *land contaminated* and introduce errors into the wind retrieval process. To enable near-coastal UHR data, the land-contaminated σ° measurements must be eliminated.

In this paper, we validate the ASCAT UHR wind estimates and determine the accuracy of the UHR data as well as the improvement in resolution of UHR winds compared with L2W winds. This is accomplished through an evaluation of the power spectra and derivative fields and a comparison with external sources, namely, data from moored buoys and from synthetic aperture radar (SAR) data.

Section II provides relevant background on ASCAT, UHR processing, and methods of analysis. Section III examines the ASCAT UHR data set, identifying its unique characteristics and quantifying its resolution enhancement over the L2W product. The processing to identify and remove land contamination is detailed in Section IV. Section V uses near-coastal buoys to compare against the L2W and UHR data. Section VI uses SAR-derived winds to validate the ASCAT UHR winds by comparing the visual characteristics, statistics, spectra, and derivative fields of the two data sets. Finally, Section VII gives conclusions from the work presented and offers suggestions for future work.

II. BACKGROUND

Wind interacts with the ocean surface, inducing small-scale capillary waves. As the wind speed increases, so does the

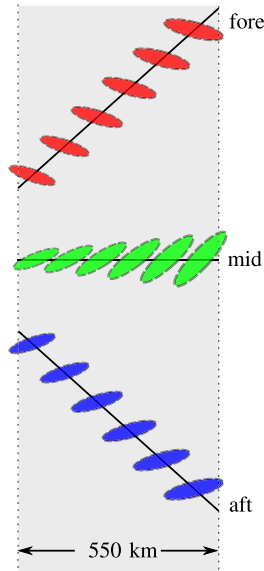


Fig. 1. Measurement geometry within each ASCAT swath (only the right swath is shown; the left swath is flipped horizontally). The ellipses represent the 3-dB contour of the SRF for the individual measurement nodes. For illustrative purposes, only a few SRFs in each beam are shown, and the SRF sizes are exaggerated.

surface roughness, which is quantified by σ° . A GMF describes the relationship of σ° with wind speed and direction for a given observation geometry (incidence and azimuth angles) [1], [2]. Multiple σ° measurements at different observation angles are required to uniquely determine the most likely vector winds for a given location. Since the collocated measurements are not exactly at the same location, they are typically resampled onto a regular grid, where each grid point is termed a wind vector cell (WVC).

A. ASCAT

An ASCAT scatterometer is hosted on the MetOp-A satellite (referred to as ASCAT-A), in operation since 2007, and on the MetOp-B satellite (referred to as ASCAT-B), in operation since 2012. ASCAT-A and ASCAT-B are identical in design and differ only in the orbit phasing of the host platforms. ASCAT measures σ° in the C-band (5.255 GHz) at vertical polarization. ASCAT uses a fan-beam antenna scheme with backscatter measurements at three azimuth angles of 45° , 90° , and 135° . Measurements are taken in each of two 550-km-wide swaths on either side of the satellite ground track. These wide swaths, separated from the ground track by about 360 km, provide measurements at an incidence angle range of 25° – 65° [3]. ASCAT covers 65% of the Earth daily and achieves near-global coverage in five days.

Within the measurement swaths, each beam is divided into 256 measurement locations, or nodes, using range-gate dechirping. Only 192 of these, however, fall into the 550-km swath and are reported. Each measurement has a corresponding footprint or measurement spatial response function (SRF). Fig. 1 shows the swath geometry, including the SRF 3-dB contour for selected measurements. The size, shape, and orientation of the SRFs vary along each beam, with a significant overlap between neighboring measurements.

The data product containing the σ° measurements for each beam is the full-resolution (SZF) level 1B (L1B). Additional L1B products that consist of spatially averaged σ° measurements on a swath-oriented grid are not considered for UHR processing. However, this swath-oriented grid is used for the L2W product with a grid spacing of 12.5 km [4].

B. UHR Processing

The current L2W product contains wind at a spatial scale adequate for many applications. However, in some cases, a wind product with a finer spatial resolution may be more beneficial, such as in near-coastal regions and storms. To accomplish this, we use UHR processing.

UHR processing is conducted on a high-resolution grid aligned with the swath-oriented 12.5-km L2W grid but subdivided into a grid with 1.25-km spacing. As with the L2W grid, each UHR grid point is referred to as a UHR WVC. The “AVE” algorithm is applied using the σ° measurements and their associated SRFs. The AVE image reconstruction method provides a limited form of resolution enhancement. The value reported at each grid point is the average of all nearby σ° measurements, weighted by each measurement’s associated SRF value at that point [5]. Following the parametric model discussed in [6], the SRF for each measurement is separately estimated. AVE reconstruction is performed separately for each of the three ASCAT beams within each swath.

UHR wind retrieval is performed using the same method as L2W: For each WVC, a maximum-likelihood estimation technique finds a wind vector solution from the three σ° values and the GMF [1]. There are often multiple maxima in the likelihood function, causing multiple ambiguous solutions [1]. One of these “ambiguities” is chosen in a postprocessing step called ambiguity selection [7]. A simple ambiguity selection scheme is used for UHR that selects the ambiguity closest to the L2W solution while retaining spatial consistency. In the interest of consistency with L2W processing, the UHR product uses code from the ASCAT Wind Data Processor (AWDP), developed by the Royal Netherlands Meteorological Institute as part of the EUMETSAT Numerical Weather Prediction Satellite Application Facility project (NWP SAF) and available at <http://nwpsaf.eu> [8]. AWDP produces L2W from the ASCAT L1B files. AWDP includes small ocean calibration corrections to σ° , which the UHR processing incorporates. As with L2W, the UHR processing uses the CMOD5.n GMF [9].

C. Land Contamination Mitigation

Each ASCAT measurement of the Earth’s surface σ° is effectively filtered through its SRF, i.e.,

$$\sigma_{\text{meas},i}^\circ = \iint \sigma^\circ(x,y) h_i(x,y) dx dy \quad (1)$$

where $\sigma_{\text{meas},i}^\circ$ is the noise-free ASCAT measurement, and $h_i(x,y)$ is the normalized SRF. The SRF is affected by the antenna pattern and the on-board processing [6]. Due to the distributed nature of the measurement SRF, a near-coastal measurement whose center is over the ocean may include σ° from

land and ocean. Land σ° is generally larger than ocean σ° . The land σ° value within the measurement footprint contaminates the ocean σ° measurement. The error due to land contamination carries through wind retrieval, so that the wind speed is overestimated.

A traditional approach to circumvent land contamination is to discard all σ° measurements within a distance threshold of land, for example, 30 km (on the order of the maximum size of an SRF). While effective, this approach is overly conservative since many measurements may lie within the distance threshold and yet be free of land contamination. This condition is common for ASCAT since the measurement footprint SRFs are elliptical.

A more informed approach is to evaluate the land contribution ratio (LCR) [10]. The LCR for measurement i is defined as

$$\text{LCR}_i = \frac{\iint L(x, y) h_i(x, y) dx dy}{\iint h_i(x, y) dx dy} \quad (2)$$

where $h_i(x, y)$ is the SRF for measurement i , and $L(x, y)$ is a binary-valued land indicator function. Since the LCR is normalized by the SRF, it varies between 0 (entirely ocean) and 1 (entirely land). In practice, the land map and SRF values are discretized on a high-resolution grid, i.e.,

$$\text{LCR}_i = \frac{\sum_{x,y} L[x, y] h_i[x, y]}{\sum_{x,y} h_i[x, y]}. \quad (3)$$

The LCR metric characterizes the degree of land contamination in a σ° measurement, depending on the accuracy of the land mask and the SRF estimate. Measurements with LCR values greater than some threshold level are discarded and not used for wind retrieval. Threshold levels for ASCAT UHR are discussed in Section IV.

D. Analysis Techniques

In this paper, we analyze the wind data using power spectra and vorticity and divergence fields. The spectra and derivative fields are also useful for comparing wind data across a range of spatial scales.

1) *Power Spectrum*: The power spectrum describes the properties of a signal in terms of the power present at different frequencies or wavenumbers. Ocean winds have a one-dimensional spatial power spectrum with an approximate slope of $k^{-5/3}$, where k is the wavenumber of the signal [11]–[13]. This is true for both the zonal and meridional components. This type of exponentially decaying spectrum is known as a “red” spectrum and follows a power law. A red spectrum implies that wind fields over the ocean are dominated, on average, by low-order characteristics and variations. This is due to an energy cascade that transfers energy from one scale to other scales through turbulence. A small increase in energy, however, can sometimes be seen in the mesoscale range (< 50 km) [13]. At very small scales, turbulence dominates, causing the spectrum to increase again, after which the energy cascade eventually dissipates into heat at the molecular scale. This process occurs at scales much smaller than are typically measured (< 20 m).

Note that the behavior described is only true on average, and any given wind field may, in fact, contain more or less energy at particular spatial frequencies than the power law would indicate. This is particularly true of extreme wind events such as storms and tropical cyclones [14] or in near-coastal areas where land features may cause jets or, otherwise, affect wind currents [15], [16].

2) *Vorticity and Divergence*: Vorticity and divergence are derived variables that describe spatial trends in the local wind velocity. According to the Helmholtz theorem, these values decompose the velocity field into rotational and irrotational components. Vorticity is defined as the curl of the horizontal wind velocity field and describes the rotational energy of the winds at any given point. Divergence measures how much a velocity field is diverging from or converging toward a given point and is the irrotational part of Helmholtz decomposition. It should be noted that on large scales, ocean wind divergence is, on average, considered to be zero. This is due to conservation of mass and the fact that wind fields on a global scale are essentially two-dimensional (2-D). In practice, however, this may not be the case in smaller regions because of noise, vertical wind movement, or other causes.

The vorticity and divergence spectra may be used as metrics for comparing wind products and analyzing ocean wind behavior. They have been previously used in modeling ocean winds and have been seen to have some power law dependence, similar to the ocean wind component spectra [11], [17]. However, if the derivative fields are computed as a first difference, the spectral behavior may depend on the spatial resolution at which the difference is performed.

III. UHR RESOLUTION ENHANCEMENT FOR ASCAT WINDS

The smaller WVC size for UHR winds compared with L2W winds permits the retrieval of higher-resolution spatial features. However, the noise content in UHR is expected to be higher, and due to the nonlinear wind retrieval, there is an uncertain improvement in the effective resolution of the UHR data. This section investigates the accuracy and validity of the resolution enhancement in UHR by comparison to the L2W data and by analyzing the noise content and visual features.

A. L2W and UHR Data Sets

While some analysis has been performed for UHR winds from other instruments [18], a detailed analysis has not been performed for ASCAT UHR winds. We begin with a visual comparison. While a visual comparison is not a rigorous validation of the data, it provides a preliminary demonstration of increased resolution.

Fig. 2 highlights the difference in spatial resolution between retrieved UHR and L2W winds for a high-wind event: Hurricane Katia of 2011. Hurricanes tend to have more high-resolution wind features than many other weather patterns due to their high wind speeds and cyclonic nature; therefore, they provide excellent case studies for comparing the resolution of two wind products [19], [20]. In Fig. 2, the UHR wind speed contours are more detailed with higher-frequency variations

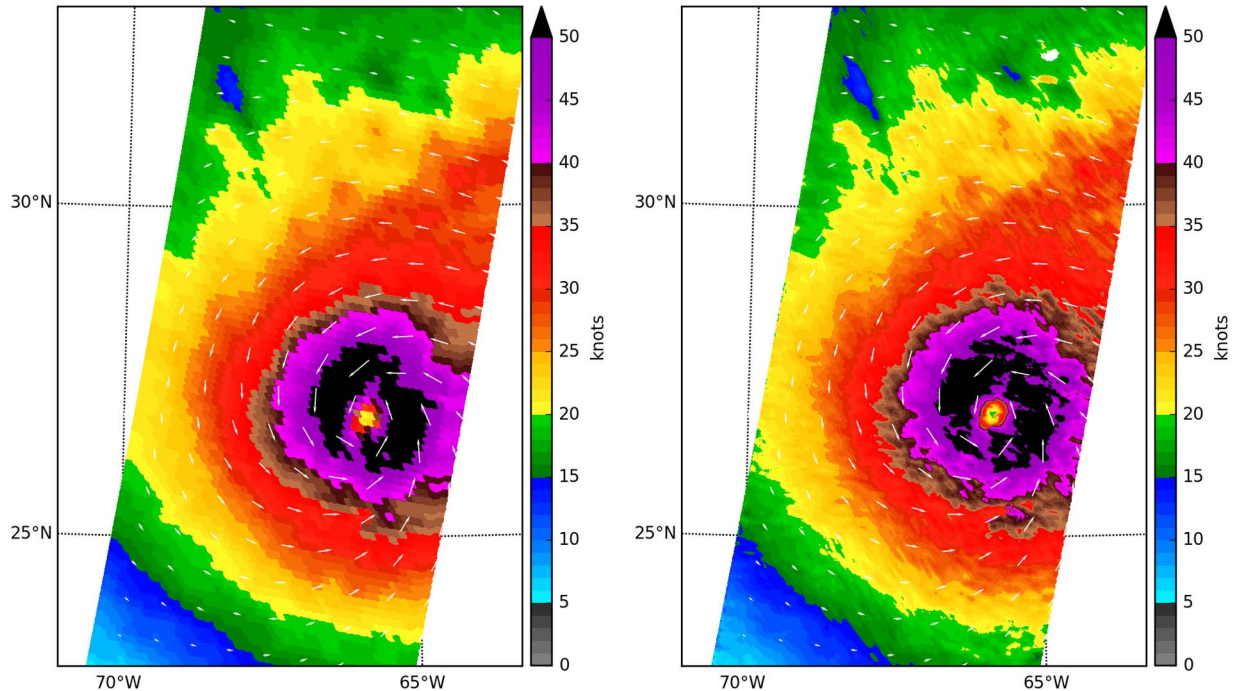


Fig. 2. (Left) L2W winds and (right) UHR winds retrieved from ASCAT on 2011-09-06 in the North Atlantic. The storm shown is Hurricane Katia. UHR data show more detail for a high-resolution wind event such as a storm. Direction arrows are downsampled to increase visibility.

than L2W. Additionally, the eye of the storm is more clearly defined in the UHR image (see [20]), and the pattern of decrease in wind speed away from the center is more detailed.

A drawback of examining storms is that the GMF used for wind retrieval is not well validated at extreme wind speeds that occur only in storms. Rain commonly associated with storms may also affect the accuracy of the retrieved winds (both UHR and L2W), although ASCAT is less affected by rain than other scatterometers because it operates in the C-band. Wind speeds above 25 m/s account for fewer than 4.3% of the total WVCs in Fig. 2. A casual comparison of the UHR and L2W wind fields reveals that there is more high-frequency information in the UHR field. This subjective observation is supported in the spectral analysis that follows in the next section.

The basic visual features and differences between L2W and UHR wind estimates show the potential benefit of using UHR data. It is difficult, however, to quantitatively analyze the resolution difference or identify the noise content solely from visual examination.

B. Overall Spectral Characteristics

As discussed in Section II, ocean winds are expected to have a red spectrum following a power law, which means that the magnitude decreases as a constant power of spatial frequency. The rate of decay is referred to as the spectral slope because when represented on a log-log scale, it is a line with constant slope. As previously noted, for ocean winds, this slope is about $k^{-5/3}$ [11], [12].

An averaged periodogram representing the zonal and meridional spectra of global UHR and L2W winds for all of the year 2011 is shown in Fig. 3, along with a $k^{-5/3}$ line for reference.

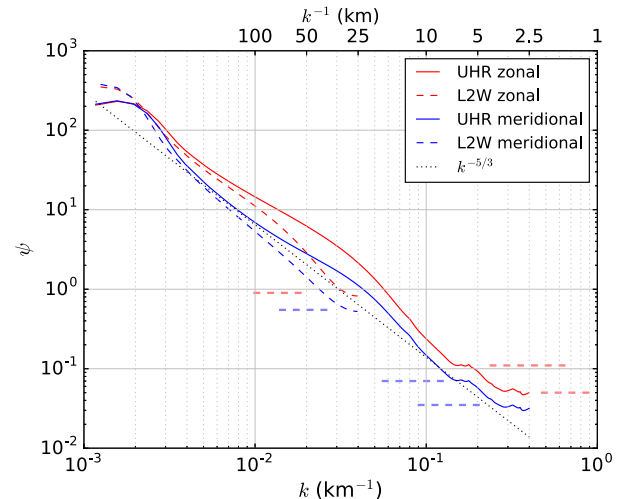


Fig. 3. UHR and L2W spectra averaged over the year 2011. The apparent noise floors for the zonal and meridional spectra discussed in the text are indicated with dashed lines next to the spectra.

The L2W spectrum approximates this reference slope, with a possible noise floor occurring at about $k^{-1} = 30$ km.

The UHR spectrum extends farther due to its higher sampling rate, but it also shows a clear extension of the spectral slope out to at least $k^{-1} = 10$ km, after which noise may distort the data. A clearly defined white noise floor is not present, but it appears that multiple levels of noise and filtering are introduced. An apparent first noise floor occurs around $k^{-1} = 8$ km, where the curve deviates from the $k^{-5/3}$ slope. Below this, the slope steepens, but around $k^{-1} = 4$ km, it flattens into a second noise floor. Some of this deviation may be due to the UHR processing algorithm, as it involves gridding and averaging measurements with irregular spacing and weighted averaging

using an estimate of the measurement SRFs. Other likely causes of deviation are thermal noise and undersampling of the wind field. The winds are likely undersampled to some degree, and because they are not band limited, the undersampling may introduce aliasing that appears as noise.

The region of the spectrum between the first and second noise floors contains at least some wind information. While ocean winds are expected to approximate the $k^{-5/3}$ spectral slope, the energy cascade can sometimes be seen to include such an increase in this mesoscale range (see Section II) [13]. Details of the spectrum at such high resolutions have not been definitively verified, however, as very few validation data sets exist. Possible physical influences on high-resolution winds include the effects of three-dimensional (3-D) wind flow. Wind fields are typically approximated as 2-D vector fields since the width of the weather-containing atmosphere is usually insignificant compared with the resolution at which wind vectors are sampled. However, the troposphere, which contains nearly all weather and wind flow, extends to an average height of about 12 km. At wavelengths smaller than this, 3-D flow may be nonnegligible. This could have an effect on the observed 2-D wind vectors and their spectra.

A comparison between the L2W and UHR spectra in Fig. 3 suggests that UHR processing improves the effective resolution of ASCAT wind estimates by at least a factor of 2 (from 25 to 10 km) based on the power law behavior. The resolution may extend further to 3 or 4 km, depending on the true characteristics of the wind spectrum at these high wavenumbers and how they compare to the spectral deviation from the power law.

Although the spectra in Fig. 3 suggest a UHR spatial resolution of 8 km, we recognize that data from many ASCAT passes are averaged together to compute the spectra, so that this inferred spatial resolution is only an average value. Due to the nonuniform sample geometry and varying sizes and orientations of the ASCAT SRFs, the true UHR spatial resolution varies. Accounting for land contamination by reducing the coastal distance threshold to 8 km may be justified, but only in an average sense. Instead, the LCR method discussed in Section II operates on a measurement-by-measurement basis so that the degree of land contamination is controlled for as precisely as the models of the SRF and land mask permit.

IV. REMOVAL OF LAND CONTAMINATION IN NEAR-COASTAL UHR ASCAT WINDS

Land contamination in the UHR data is addressed through the LCR, as previously discussed. The LCR is evaluated using the SRF for each measurement and a binary land map, rasterized to a grid spacing of $1/100^\circ$. To avoid land contamination entirely, all measurements with a nonzero LCR should be discarded and not used for wind retrieval. However, to increase the amount of retrievable near-coastal winds, this strict threshold is relaxed; measurements with a small amount of land contamination are permissible so long as the impact of land contamination on the estimated wind is small.

Based on trial and error with some case studies, a reasonable LCR threshold is -20 dB. However, this threshold level is subjective. The more objective approach discussed in this section

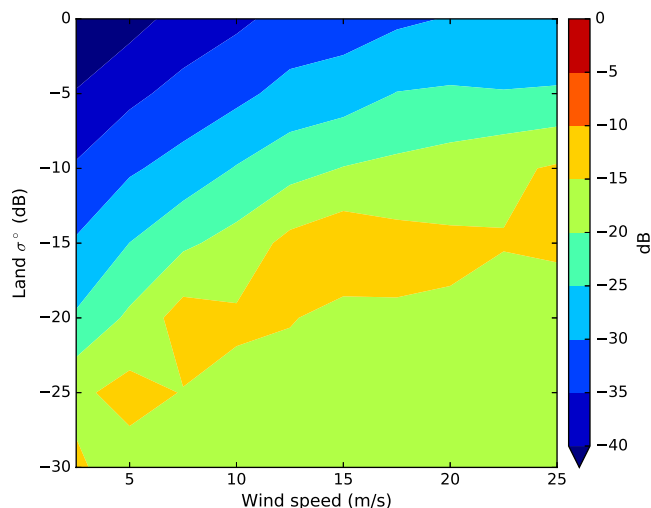


Fig. 4. For a WVC, the largest LCR value such that the land contamination error is within 10% of the ocean-only rms wind speed error. The LCR value is a function of wind speed, land σ° , and WVC.

is to choose the threshold level subject to minimizing a suitable error metric. This approach also allows the LCR threshold to vary as a function of local conditions.

Our approach with ASCAT is similar to previous work with QuikSCAT land contamination [10]. The QuikSCAT LCR threshold is evaluated using compass simulations and found to be largely a function of local land σ° , local wind speed, and cross-track position. We find that this evaluation also holds for ASCAT.

The compass simulation procedure [10] is to define a “truth” wind field with spatially constant speed and direction. The scatterometer measurement geometry and GMF are used to sample the truth wind field to create synthetic σ° measurements. Wind retrieval is performed using these σ° values, and the retrieved winds are compared with the original truth wind field. This process is repeated for multiple wind speeds and directions to evaluate the retrieval performance over a variety of parameters. Land contamination is additionally modeled in the compass simulation by including a land σ° value and an LCR value (for each simulation run, both are constant over the entire synthetic input field). To give the worst-case error, each simulated LCR value is equally applied in all beams.

We perform the compass simulations for ASCAT for a range of wind speeds, directions, land σ° values, and LCR values. The simulation outputs are used to determine a dynamic LCR threshold. As an intermediate step in creating a dynamic LCR threshold, first, a root mean square (rms) wind speed error threshold is determined.

Because the rms wind speed error increases as a function of true wind speed, we use a relative threshold. First, the ocean-only error is determined by computing the rms wind speed error with no land contamination present. The error threshold is defined such that the total rms wind speed error is set so that the additional error due to land contamination is no greater than 10% of the ocean-only error. We select a 10% error threshold since the total speed error, even at wind speeds of 25 m/s, is less than 1.0 m/s. The maximum error due to land contamination alone is therefore less than 0.09 m/s.

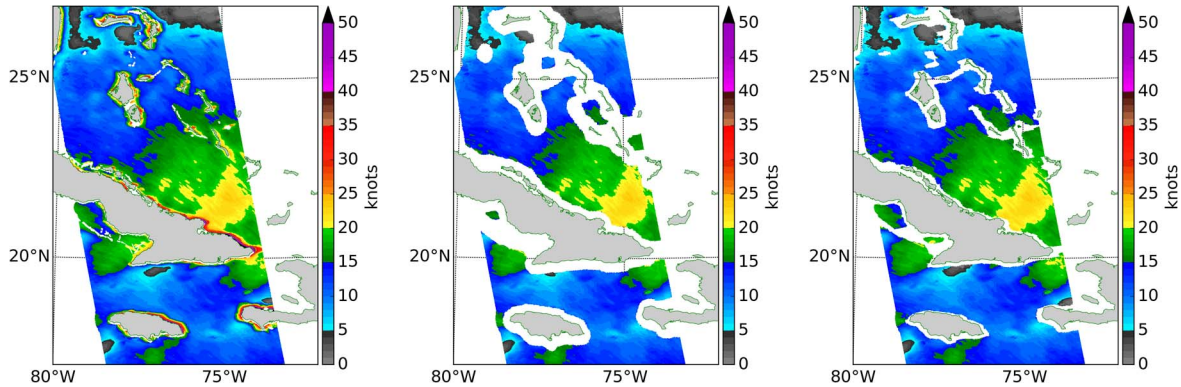


Fig. 5. UHR winds (left) with no land contamination mitigation, (center) with a distance threshold of 30 km, and (right) with a dynamic LCR threshold. ASCAT-A data are from an ascending pass on 2013-02-05, orbit 32682, right swath.

From this rms speed error threshold, the LCR error threshold is determined. The LCR error threshold is the LCR value such that the corresponding rms speed error is less than the error threshold (10% of the ocean-only error). The LCR threshold is a function of 1) local wind speed, 2) local land σ° , and 3) cross-track location. The threshold values are stored as a lookup table to determine the maximum LCR threshold such that the additional wind speed rms error due to land is, at most, 10% of the ocean-only error. The local wind speed and land σ° are determined for each measurement by averaging nearby L2W wind speeds and land σ° values for each near-coastal measurement. The cross-track location is given in terms of the nearest L2W WVC.

A selection from the LCR lookup table is shown in Fig. 4 for a single cross-track position. Values for other cross-track locations are similar but somewhat vary. For low wind speeds and low land σ° values, a modest LCR threshold level may be used (≈ -20 dB). As the wind speed increases (moving left to right along Fig. 4), an increasing LCR threshold is required to maintain the maximum rms speed error (the absolute speed error also increases as the wind speed increases since the rms speed error threshold is a percentage of the ocean-only error). Similarly, as the land σ° decreases (moving top to bottom along Fig. 4), generally, a larger (although not monotonically increasing) LCR level is allowable, since the impact of land contamination decreases.

To illustrate land contamination mitigation using a dynamic LCR threshold, we show UHR wind speeds in Fig. 5 for a Caribbean region containing many islands and coastlines. Three cases of UHR are produced: with no land contamination mitigation, with a distance threshold of 30 km, and with a dynamic LCR threshold. The mean LCR threshold level for this case is -25.2 dB, but, due to differing nearby land σ° levels and wind speeds, the threshold varies from -38.1 to -6.2 dB, with a standard deviation of 4.9 dB.

As expected, with no attempt to avoid land contamination, the wind speeds near land in Fig. 5 are biased high. A distance threshold of 30 km is effective at removing land contamination, but it removes all near-coastal measurements, contaminated or not. The dynamic LCR threshold approach permits retrieval much closer to land, with no visible wind speed biases. For this region, of all valid WVCs within 30 km of land, 50% are within 18 km, and 10% are 8 km or closer.

We note that even with the land contamination approach used here, the distribution of retrieved winds near land may differ from those over open ocean. This is attributed to residual undetected land contamination or to geophysical effects, since the actual near-coastal wind may not be neutrally stable or be otherwise affected by land. For these reasons, we then compare the UHR wind estimates with near-coastal buoy data.

V. VALIDATION OF ASCAT NEAR-COASTAL UHR USING BUOY DATA

To validate the near-coastal UHR wind data, we compare ASCAT winds with buoy-measured winds. Buoy data distributed by the National Oceanic and Atmospheric Administration (NOAA) Marine Environmental Buoy Database¹ are used. We select buoys in a region along the North American coastline of the Atlantic Ocean where buoys are present at a variety of distances from land. The buoy locations and identification numbers are shown in Fig. 6.

To compare the buoy-measured winds with ASCAT wind estimates, the buoy-measured winds are converted into neutrally stable wind speeds at a standard height of 10 m above sea level to match the ASCAT winds. We use the Liu–Katsaros–Businger model [21], [22], which requires other buoy-measured quantities including air and sea temperatures and relative humidity. Only buoy measurements with sufficient quality-controlled information are used. Since the accuracy of both ASCAT and buoy measurements degrades at low wind speeds, we do not include wind speeds below 5 m/s.

Passes from both ASCAT-A and ASCAT-B are used to find collocations between the buoys and the ASCAT instruments. All ASCAT UHR WVCs within 10 km of the reported buoy location are averaged together. Because the buoy winds are reported every 10 min, the largest temporal difference between a collocation is 5 min.

The buoy and ASCAT collocations are collected for the date range from 2014-07-01 to 2015-06-30. In addition to L2W winds, three variations of UHR processing are included: UHR-`none`, which does not perform any land contamination mitigation; UHR-`mdl`, which discards all σ° measurements

¹<https://www.nodc.noaa.gov/BUOY/>

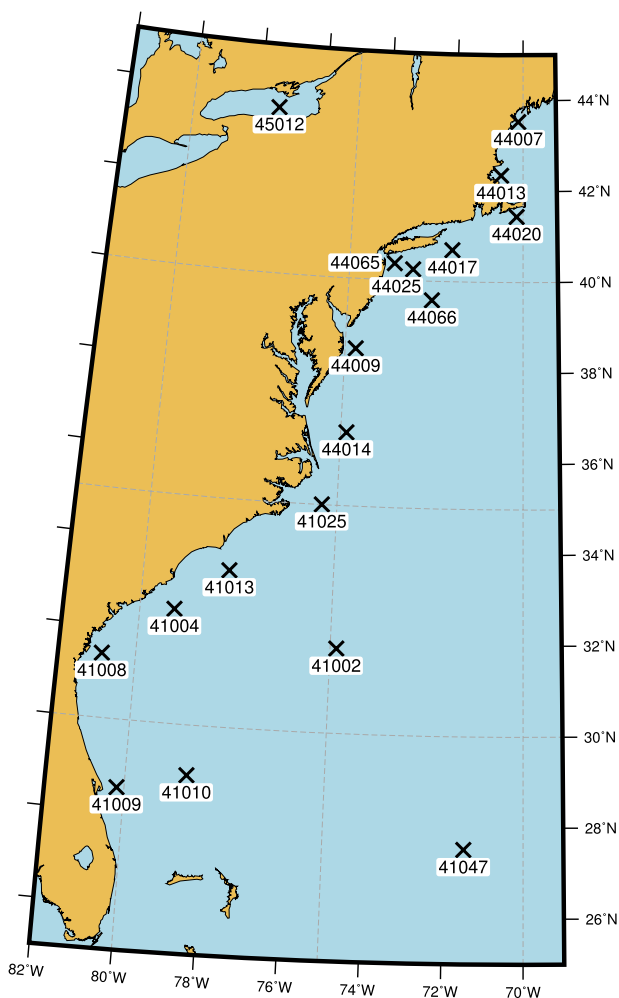


Fig. 6. Buoy locations and identification numbers used for near-coastal validation.

within 30 km of land from UHR processing; and UHR-*lcr*, which uses LCR processing with a dynamic LCR threshold.

The L2W product has been previously validated using buoy measurements [23]. We expect our comparison to yield similar results. The UHR-*none* product is expected to perform poorly near land due to land contamination, but it has the greatest number of collocations. The UHR-*mdl* represents a best-case situation where no land contamination is present, but it has a reduced number of collocations. We anticipate the UHR-*lcr* product to have similar statistics as the L2W and UHR-*mdl* cases, but with an increased number of collocations.

A comparison of the ASCAT and buoy wind speeds is shown in Fig. 7 for all four cases. The tendency of ASCAT winds to slightly underestimate high wind speeds has been previously noted [23]. Land contamination is readily visible in the UHR-*none* case, in which many ASCAT wind speeds that are higher than the buoy wind speeds are present. The other three cases are very similar to each other, although the UHR-*mdl* and UHR-*lcr* correlation coefficient and slope fit the buoy data slightly better than do the L2W data. For brevity, we do not display the wind direction comparison, but note that with respect to the collocations between ASCAT and the selected buoys, land contamination does not affect wind direction as

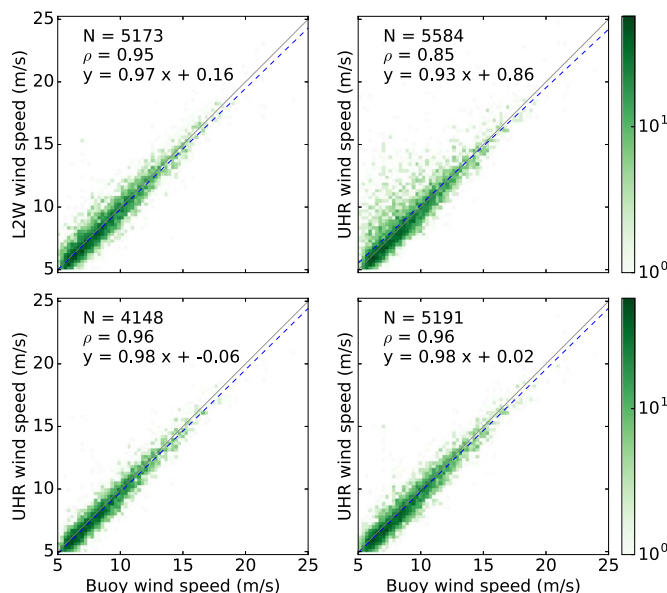


Fig. 7. Collocated ASCAT wind speeds compared with buoy wind speeds. The number of collocations (N), correlation coefficient (ρ), and linear fit ($y = mx + b$) are shown for each case. (Top left) L2W; (top right) UHR-*none*; (bottom left) UHR-*mdl*; (bottom right) UHR-*lcr*.

strongly as it does wind speed. The comparison of UHR and buoy wind directions is very similar to the L2W comparison.

The wind speed residual, or the difference between buoy and ASCAT wind speeds, is also computed. For bins of buoy wind speeds, the mean and the standard deviation of the residuals are shown in Fig. 8. As before, the large bias and standard deviation for the UHR-*none* case, particularly at low wind speeds, are evidence of land contamination. The means and standard deviations for the other three cases are very similar to each other, although the L2W product has a larger bias at buoy wind speeds of about 5 m/s, which is also present—and larger—for UHR-*none*. This bias is due to land contamination and is not present for UHR-*mdl* nor UHR-*lcr*.

Finally, the wind speed residuals (buoy-ASCAT) are shown in Fig. 9 as a function of distance to land. The results greater than about 20 km are identical, indicating that land contamination is not present at these distances. Within 20 km of land, the UHR-*none* product has both a large bias and an error standard deviation that increase as the distance to land decreases. The L2W case, on the other hand, has a bias within 1 m/s consistently for all coastal distances. The UHR-*lcr* product has collocations with 20 km, and the bias and standard deviations are similar to the L2W results.

Based on these collocations with near-coastal buoy measurements, we find that the LCR method is effective at removing land contamination while retaining a large number of uncontaminated near-coastal wind estimates. With no land contamination mitigation, the UHR product overestimates the wind speeds and increases the retrieval error. In both the UHR-*mdl* and UHR-*lcr* cases, the statistics of the comparisons with buoy winds are very similar to the conventional-resolution L2W winds. That is, no evidence suggests that the UHR winds are noisier or contain more error with respect to the buoys. In fact,

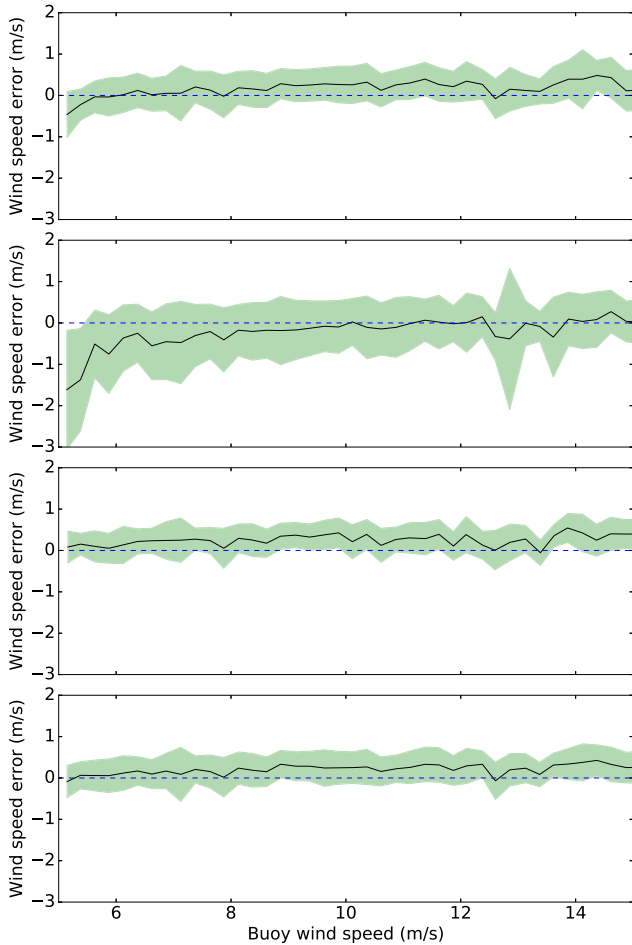


Fig. 8. Mean (solid lines) and standard deviation (shaded region) of the difference between buoy wind speeds and ASCAT. (Top to bottom) L2W, UHR-none, UHR-MDL, and UHR-LCR.

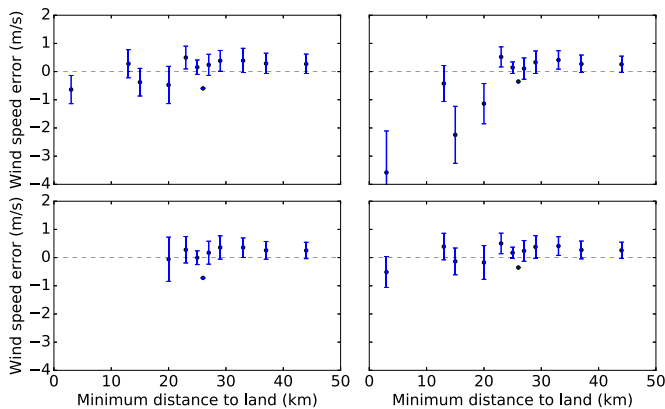


Fig. 9. As a function of distance to land, the mean and standard deviation of the difference between buoy wind speeds and ASCAT. (Top left) L2W; (top right) UHR-none; (bottom left) UHR-MDL; and (bottom right) UHR-LCR.

the residual speed error statistics are a little lower for UHR than for L2W.

While the buoy measurements provide consistent point measurements of the wind field, they are too sparsely sampled to have a comparable spatial resolution with ASCAT data. To validate the spatial resolution of UHR data, we use an additional data set: SAR-derived wind estimates, which are considered in the following section.

VI. VALIDATION OF ASCAT UHR USING SAR WIND DATA

Over the open ocean, the available wind speed comparison data at the coverage and spatial resolution of a scatterometer are limited. One source examined in this section is near-surface ocean wind speeds measured by a SAR. Not only do SAR-derived winds have coverage comparable to a scatterometer in some areas, but the spatial resolution of the SAR σ° measurements is much finer than for a scatterometer.

This section first provides a basic overview of the SAR wind product used to validate the ASCAT UHR wind data. The collocation procedure is discussed, following which a comparison is made between the two data sets.

A. SAR Winds

As with scatterometers, wind vector estimates can be retrieved using the GMF and the measured SAR σ° . However, SAR σ° measurements are typically available only at a single azimuth angle, which is insufficient to uniquely invert the GMF to find the most likely wind speed and direction. The wind direction is instead obtained in one of two ways. The first is from an external source such as numerical weather models, and the second uses linear features in the SAR σ° image itself. There are tradeoffs between these two methods. The linear features in the SAR images are not always present and may be affected by other atmospheric and oceanographic conditions, and model wind directions are usually at a much lower resolution than SAR data [15], [24], [25].

For SAR wind data, we use the Advanced SAR (ASAR) of the European Space Agency's Environmental Satellite (ENVISAT) mission. ENVISAT is an Earth-observing satellite that includes many other remote sensing instruments used in environmental studies. The mission lasted from March 2002 to April 2012, providing nearly five years of overlap with ASCAT. ASAR operates in the C-band, as does ASCAT.

ASAR near-surface wind estimates are acquired from the Alaska SAR Demonstration Project (AKDEMO), provided by NOAA [26]. These data are retrieved on a 0.5-km grid using the CMOD5 GMF. The accuracy of SAR winds from this project is validated through systematic comparison to National Data Buoy Center buoy wind speeds, model wind speeds, and QuikSCAT scatterometer wind speeds [24], [25]. In these studies, the standard deviation of SAR winds is found to be 1.76 m/s from buoy winds and 1.78 m/s from QuikSCAT winds.

The ASAR wind directions are from the Navy Operational Global Atmospheric Prediction System (NOGAPS), which are posted on a 1° grid. Although the ASAR wind speeds are at the high spatial resolution of ASAR, because the wind direction is not retrievable with SAR, the spatial resolution of the wind direction data is at the much more coarse resolution of the NOGAPS wind model. We note that this limitation may affect our analyses below when ASAR wind direction information is used.

Another limitation of the ASAR data is due to the GMF. ASAR winds are retrieved using the CMOD5 GMF. This GMF is an empirical fit derived for scatterometers such as ASCAT and has not been validated for the spatial scales observed by ASAR. Thus, errors in the retrieved ASAR wind speeds may



Fig. 10. Locations of 105 ASCAT/ASAR collocations between 2010-05-01 and 2011-08-31.

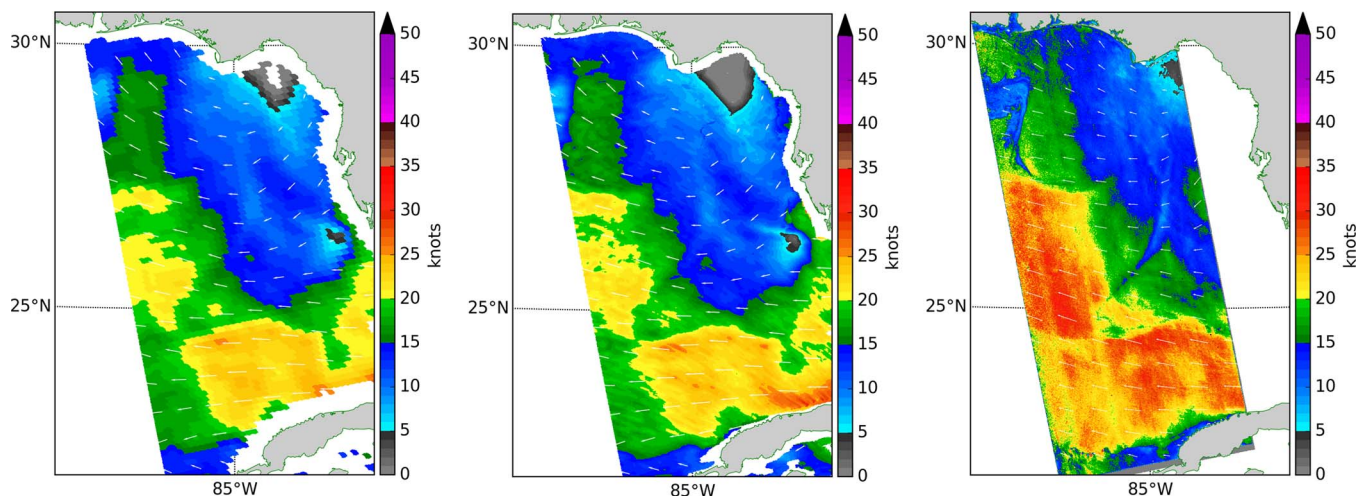


Fig. 11. Collocated (left) L2W, (middle) UHR, and (right) ASAR winds retrieved on 2010-05-15 at 3:12:00 UTC (ASCAT) and at 3:42:55 UTC (ASAR). Direction arrows are downsampled to increase visibility.

be present, particularly at the finer spatial scales. Furthermore, the GMF used to retrieve ASAR winds (CMOD5) differs from the GMF used for ASCAT (CMOD5.n), both UHR and L2W, where the primary difference between the two GMFs is a bias of 0.7 m/s [9]. Notwithstanding the different GMFs used between ASAR and ASCAT, we expect that differences in retrieved wind fields are dominated more by the sensor geometries and limitations.

The number of collocations between ASCAT and ASAR is limited. The orbits of the host satellites (MetOp-A and ENVISAT, respectively) differ, but on occasion, the ground swaths of ASCAT and ASAR sufficiently overlap. Unfortunately, the AKDEMO does not provide wind estimates for all ASAR data but, instead, provides only example wind fields, mostly focusing on certain near-coastal areas in North America [16]. This limits the number of collocations available for this study.

The criteria for selecting ASCAT/ASAR collocations include 1) less than a one-hour time offset between ASAR and ASCAT data and 2) a spatial overlap of the two swaths of several degrees in both latitudinal and longitudinal directions. We find 105 such collocations between 2010-05-01 and 2011-08-31, with locations indicated in Fig. 10. Our collocation procedure does not

select for similar radar incidence angles; hence, the collocated winds may be observed by very different incidence angles.

B. Example Collocation

One particular collocation, shown in Fig. 11, shows ASAR and ASCAT winds with a time offset of about 30 min and covering almost identical areas. In Fig. 11, there is a clear progression toward higher spatial resolution moving from L2W to UHR to SAR. Similar low-resolution features are visible in all three images, providing evidence that the three data sets are consistent at large scales. The high-resolution features and characteristics in the SAR and UHR winds are fairly consistent, although not identical.

In the high-wind-speed area around 24° N 85° W, while the L2W winds show little variation, the UHR winds contain more peaks and dips. More importantly, the UHR peaks and dips are consistent with those in the SAR image. The center of the wind field contains a transition between low and high wind speeds, visible in all three cases. This transition area has attributes that are much more detailed in the UHR and SAR fields than in the L2W field. These details are similar across the two

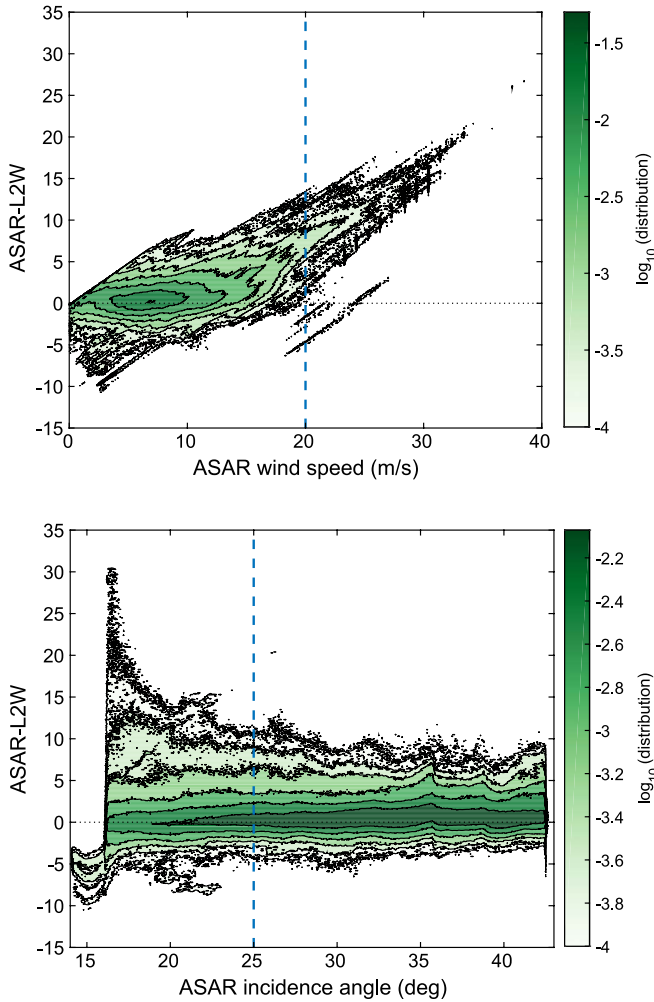


Fig. 12. Two-dimensional histograms of the difference in ASAR and L2W wind speeds versus (top) ASAR wind speed and (bottom) ASAR incidence angle. At high wind speeds or at low incidence angles, ASAR data are too noisy and are excluded from analysis. Results comparing UHR wind speeds with ASAR are very similar.

high-resolution data sets, providing more evidence of the accuracy of the UHR data set. However, the SAR wind field appears to contain higher wind speeds and has some high-resolution features that do not appear in the other two cases.

This example collocation illustrates that the additional high-frequency content in UHR data not present in the L2W data is often confirmed by the SAR data. Of course, the SAR data have features not present in the ASCAT data. We note the 30-min time difference between the ASAR and ASCAT observations, which could contribute to some differences. For further analysis, statistical and spectral data are used to examine the wind estimates.

C. Wind Speed Comparison

Here, the collocated L2W, UHR, and ASAR wind speeds are compared. The wind speed differences between L2W and ASAR speeds as a function of ASAR wind speed and of the ASAR incidence angle are shown in Fig. 12. The comparison using UHR wind speeds is similar but is not shown. The wind

TABLE I
STATISTICS OF THE COLLOCATED UHR, L2W, AND ASAR WIND SPEEDS. 10 440 657 TOTAL COLLOCATED MEASUREMENTS EXIST, BUT WITHIN THE WIND SPEED AND INCIDENCE ANGLE RANGE DISCUSSED IN THE TEXT, THIS REDUCES TO 7 595 802 COLLOCATIONS. ALL UNITS ARE IN METERS PER SECOND

All Data	ASAR	ASCAT UHR	ASCAT L2W
Mean	8.512	7.327	7.318
Median	7.663	7.025	7.033
Std. Dev.	4.827	3.663	3.610
Within Range			
Mean	8.158	7.169	7.155
Median	7.635	6.919	6.911
Std. Dev.	3.834	3.557	3.507

speed residual is low, indicating that the ASCAT and ASAR wind speeds agree well with each other. However, the variance and bias increase as the ASAR wind speed increases. The variance of the wind speed residual also increases for low incidence angles.

The GMF used to retrieve winds is not well validated at high wind speeds. Furthermore, the high wind speeds estimated from ASAR data may be affected by fine-scale oceanographic effects that are observed at SAR resolution but not observable to ASCAT and are therefore not modeled by the GMF. Wind speeds greater than 20 m/s are excluded in this study, as indicated by the vertical dashed line in Fig. 12.

Additionally, the CMOD5 GMF is not well validated for low incidence angles (below about 25°); however, ASAR data contain measurements at incidence angles as low as 14° . It has been found in previous studies that at very low incidence angles, the expected inverse relationship between SAR incidence angle and σ° does not hold. This may cause both σ° and wind speed values to be lower than as predicted [24], [25]. In this paper, all data points with an ASAR incidence angle of less than 25° are excluded from analysis, shown in Fig. 12 as the vertical dashed line. This cutoff corresponds to the ASCAT incidence angle range, as well as that used in [24] and [25].

Statistics for the collocated ASAR and ASCAT data sets are shown in Table I, both before and after excluding data from outside the acceptable wind speed and incidence angle ranges. The largest change is the decrease in the standard deviation of the ASAR speeds. The ASCAT UHR and L2W statistics are similar to each other in all cases.

Fig. 13 shows joint distributions between the ASCAT and ASAR wind speeds, with their relative statistics summarized in Table II. The distributions for L2W and UHR are very similar to each other, and they both exhibit a strong linear trend, indicating that the ASCAT and ASAR wind speeds largely agree with each other. However, the wind speeds appear to be somewhat overestimated by ASAR with respect to the ASCAT wind speeds. The correlation coefficient, standard deviation, and mean difference between UHR and ASAR are slightly better than those between L2W and ASAR, but the improvement is essentially negligible.

It is significant that the wind speeds from both ASCAT products (L2W and UHR) equally agree with the ASAR wind speeds. Although the UHR wind speeds are expected to be somewhat noisier than the L2W speeds, there is very little

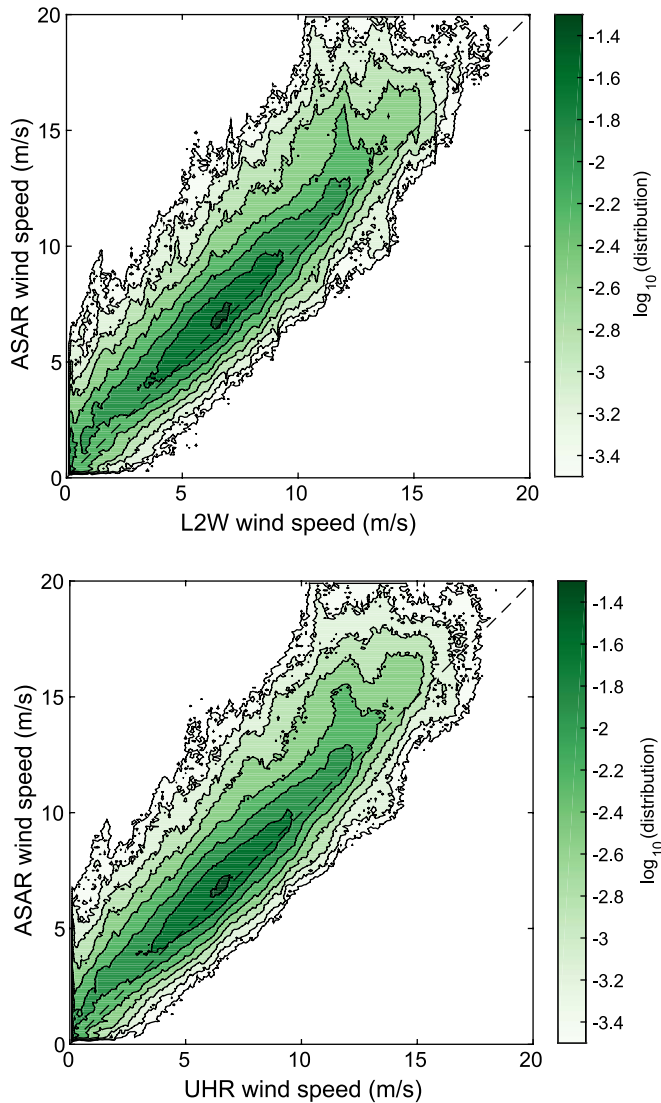


Fig. 13. Distributions of ASAR wind speed values versus (top) L2W and (bottom) UHR. ASAR wind speeds > 20 m/s and incidence angles $< 25^\circ$ are excluded.

TABLE II

STATISTICS FOR 7 595 802 COLLOCATED ASAR AND ASCAT WIND SPEEDS. AS DESCRIBED IN THE TEXT, ASAR WIND SPEEDS > 20 m/s AND INCIDENCE ANGLES $< 25^\circ$ ARE EXCLUDED. UNITS FOR STANDARD DEVIATION AND MEAN DIFFERENCE ARE IN METERS PER SECOND

Datasets	Correlation Coef.	Std. Dev.	Mean Diff.
L2W/ASAR	0.895	1.985	1.002
UHR/ASAR	0.896	1.976	0.989

difference with respect to ASAR wind speeds. This indicates that the additional information in UHR is just as consistent with ASAR as is L2W.

D. Power Spectra

Computing the power spectra of the different data sets permits comparison at different spatial scales. Fig. 14 shows the average zonal and meridional wind spectra for ASCAT L2W, ASCAT UHR, and ASAR winds over all 7 595 802 collocations

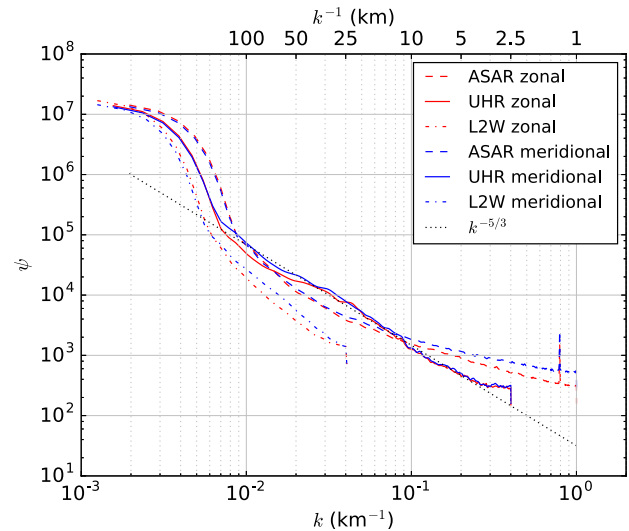


Fig. 14. L2W, UHR, and ASAR wind zonal and meridional spectra averaged over all 7 595 802 collocations. A $k^{-5/3}$ slope is shown for reference.

in 105 cases (ASCAT passes). The spectra all have the similar overall trend of power law decay. However, there are significant differences as the wavenumber increases. The L2W spectra slope downward slightly steeper than the reference $k^{-5/3}$ slope. The UHR spectra, however, follow the reference $k^{-5/3}$ slope closely until about $k^{-1} = 4$ km. The ASAR spectra have the shallowest slope, dropping below the UHR spectra for the mid-range wavenumbers and rising back above for the highest wavenumbers.

UHR winds consist of wind direction estimates at the same resolution as the estimated wind speeds. Therefore, when combining both estimated wind speed and direction into zonal and meridional components, the UHR spectra use two high-resolution data sets, whereas the ASAR data use high-resolution (σ° measurements) and low-resolution (external wind direction information) data sets. This may explain why the ASCAT wind component spectra are more representative of the expected ocean wind spectrum than are the ASAR spectra.

E. Vorticity and Divergence

A comparison of the vorticity and divergence spectra for each wind data set helps validate UHR winds. However, since each data set is retrieved at a different grid resolution, the first-order differences are taken across unequal distances. The magnitude and behavior of the vorticity and divergence spectra may therefore vary based on the spatial scale at which they are calculated. For this reason, the higher-resolution data sets (UHR and SAR) are resampled at several different resolutions before calculating vorticity and divergence.

The vorticity and divergence spectra are shown in Figs. 15 and 16 with similar results. Each figure shows the spectrum for each data set resampled at various grid resolutions. As the ASAR winds are increasingly downsampled, the spectra decrease in power and taper off at higher wavenumbers. The UHR spectra (at the nonresampled pixel size of 1.25 km) are located between the SAR spectra resampled at 1.5 and 2 km.

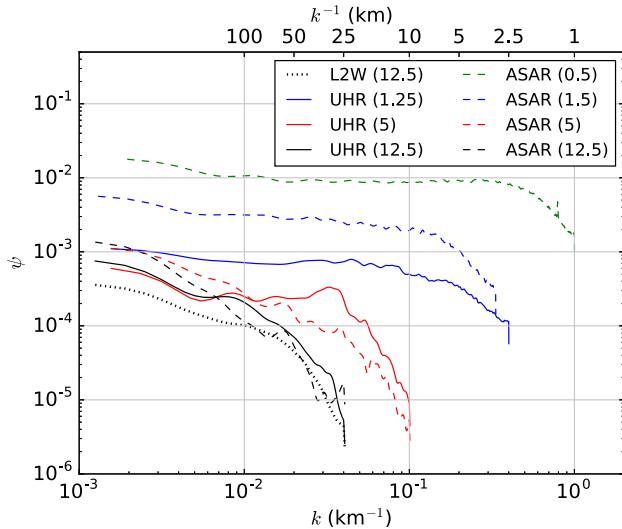


Fig. 15. Vorticity spectra for L2W, UHR, and ASAR winds, with the UHR and ASAR data resampled at various sizes. The quantities in parentheses in the legend indicate the pixel size in kilometers at which the vorticity is calculated.

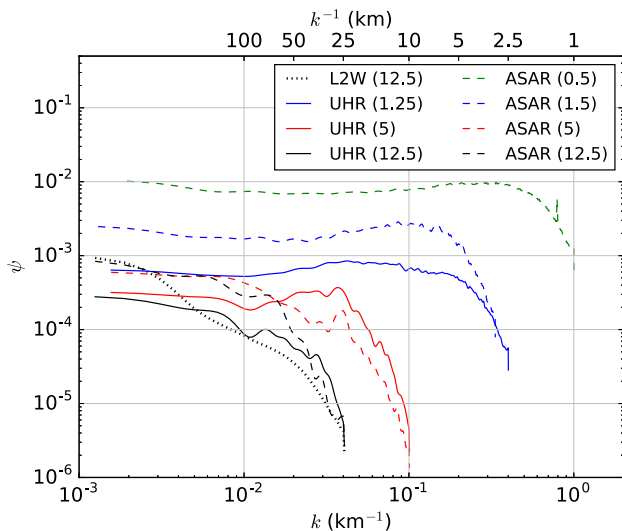


Fig. 16. Divergence spectra for L2W, UHR, and ASAR winds, with the UHR and ASAR data resampled at various sizes. The quantities in parentheses in the legend indicate the pixel size in kilometers at which the divergence is calculated.

This suggests that the effective resolution of the UHR winds is on the order of 4 km.

The UHR and SAR spectra match fairly well when the vorticity and divergence are calculated at the same grid resolutions, for example, at the 5- and 12.5-km lines in the figures. Both the power level and shape of the spectra are very similar, although there is evidence of sidelobes due to the spatial averaging performed when resampling the data. Additionally, both the UHR and SAR spectra are very similar to the L2W spectrum at the 12.5-km grid resolution. These results validate the consistency of the derivative fields of all three data sets when analyzed at matching grid spacings. This suggests that the data itself is consistent and that ASCAT UHR winds provide valid high-resolution wind data down to a spatial resolution as fine as 4 km.

VII. CONCLUSION

The ASCAT UHR winds presented in this paper agree very well with the conventional L2W wind product. The results indicate that UHR winds are consistent with L2W winds and with higher-resolution SAR-derived winds. A tradeoff between resolution enhancement and additional noise is expected; however, we find that the additional noise in UHR winds is mainly evident at the highest frequencies. At larger scales, UHR winds are very similar to L2W winds.

The results presented in this paper show that UHR winds contain valid information at finer scales than L2W winds. Although the resolution improvement of ASCAT UHR winds is difficult to precisely quantify due to a lack of truth data, the results obtained suggest the UHR product contains valid wind data down to scales of 10 km, and possibly down to scales of 4 km. This is an improvement over the nominal 25-km resolution of the L2W winds and suggests that ASCAT UHR wind data may be useful for applications that require wind vectors on a finer scale.

Over the open ocean, we validate ASCAT UHR winds through comparison with SAR-derived winds. The comparison highlights the presence of common fine-scale features, the similarity of the UHR statistics to that of L2W and SAR despite being compared on a finer scale, the compatibility of the UHR product with the expected spectral properties of ocean winds, and the similarity of the derivative fields in both data sets.

For near-coastal areas, ASCAT UHR winds are validated through comparison with buoy measurements. The LCR is used to discard land-contaminated ocean σ° measurements while precisely controlling the amount of error tolerable in the final retrieved winds. The buoy comparison reveals the large errors present in ASCAT UHR winds when no land contamination mitigation is attempted and shows that with the LCR method, there is no evidence of land contamination in the UHR data. Using the LCR method, ASCAT wind retrieval within a few kilometers of land is now possible.

Future work could extend the coastal buoy analysis. More buoys could be included and the data collected over a longer time scale. Additionally, although the ASAR winds are at a high enough resolution to be compared with the ASCAT UHR winds, the limitations of the ASAR winds, particularly the unvalidated GMF at scales finer than 10 km, indicate that an alternate high-resolution data set should be used in the future.

The ASCAT UHR wind product may continue to be analyzed, validated, and improved. For example, rain may be simultaneously retrieved from the σ° measurements as well as wind [27], [28]. Another possible improvement is model-based ambiguity selection, which may decrease incorrect ambiguity selections in the UHR product and provide a more accurate and self-consistent product [29].

REFERENCES

- [1] F. T. Ulaby and D. G. Long, *Microwave Radar and Radiometric Remote Sensing*. Ann Arbor, MI, USA: Univ. Michigan Press, 2014.
- [2] H. Hersbach, A. Stoffelen, and S. de Haan, "An improved C-band scatterometer ocean geophysical model function: CMOD5," *J. Geophys. Res., Oceans*, vol. 112, no. C3, 2007, Art. no. c03006.

- [3] J. Figa-Saldaña, J. J. W. Wilson, E. Attema, R. Gelsthorpe, M. R. Drinkwater, and A. Stoffelen, "The Advanced Scatterometer (ASCAT) on the Meteorological Operational (MetOp) platform: A follow on for European wind scatterometers," *Can. J. Remote Sens.*, vol. 28, no. 3, pp. 404–412, Jun. 2002.
- [4] "ASCAT wind product user manual, Version 1.13," KNMI, De Bilt, The Netherlands, May 2013. [Online]. Available: http://projects.knmi.nl/scatterometer/publications/pdf/ASCAT_Product_Manual.pdf
- [5] R. D. Lindsley and D. G. Long, "Enhanced-resolution reconstruction of ASCAT backscatter measurements," *IEEE Trans. Geosci. Remote Sens.*, vol. 54, no. 5, pp. 2589–2601, May 2016.
- [6] R. D. Lindsley, C. Anderson, J. Figa-Saldaña, and D. G. Long, "A parameterized ASCAT measurement spatial response function," *IEEE Trans. Geosci. Remote Sens.*, vol. 54, no. 8, pp. 4570–4579, Aug. 2016.
- [7] M. P. Owen and D. G. Long, "Simultaneous wind and rain estimation for QuikSCAT at ultra-high resolution," *IEEE Trans. Geosci. Remote Sens.*, vol. 49, no. 6, pp. 1865–1878, Jun. 2011.
- [8] A. Verhoef, J. Vogelzang, J. Verspeek, and A. Stoffelen, "AWDP user manual and reference guide, Version 2.3," KNMI, De Bilt, The Netherlands, Feb. 2014.
- [9] H. Hersbach, "Comparison of C-band scatterometer CMOD5.n equivalent neutral winds with ECMWF," *J. Atmos. Ocean. Technol.*, vol. 27, no. 4, pp. 721–736, Apr. 2010.
- [10] M. P. Owen and D. G. Long, "Land-contamination compensation for QuikSCAT near-coastal wind retrieval," *IEEE Trans. Geosci. Remote Sens.*, vol. 47, no. 3, pp. 839–850, Mar. 2009.
- [11] M. H. Freilich and D. B. Chelton, "Wavenumber spectra of Pacific winds measured by the Seasat scatterometer," *J. Phys. Oceanography*, vol. 16, no. 4, pp. 741–757, Apr. 1986.
- [12] D. G. Long and D. D. Luke, "The wavenumber spectra of scatterometer-derived winds," in *Proc. IEEE Int. Geosci. Remote Sens. Symp.*, Houston, TX, USA, May 1992, pp. 1005–1007.
- [13] I. Van der Hoven, "Power spectrum of horizontal wind speed in the frequency range from 0.0007 to 900 cycles per hour," *J. Meteorol.*, vol. 14, no. 2, pp. 160–164, Apr. 1957.
- [14] F. Saïd, "An evaluation of quickscat uhr wind product's effectiveness in determining selected tropical cyclone characteristics," Master's thesis, Brigham Young Univ., Provo, Utah, USA, 2009.
- [15] F. M. Monaldo, D. R. Thompson, N. S. Winstead, W. G. Pichel, P. Clemente-Colón, and M. B. Christiansen, "Ocean wind field mapping from synthetic aperture radar and its application to research and applied problems," *Johns Hopkins APL Tech. Dig.*, vol. 26, no. 2, pp. 102–113, 2005.
- [16] W. G. Pichel *et al.*, "ENVISAT ASAR applications demonstrations: Alaska SAR demonstration and Gulf of Mexico hurricane studies," in *Proc. Envisat Symp.*, Montreux, Switzerland, 23–27, Apr. 2007, pp. 1–6.
- [17] J. Gunther and D. G. Long, "Models for the near-surface oceanic vorticity and divergence," in *Proc. IEEE Int. Geosci. Remote Sens. Symp.*, Pasadena, CA, USA, 8–12, Aug. 1994, pp. 951–953.
- [18] A. M. Plagge, D. C. Vandemark, and D. G. Long, "Coastal validation of ultra-high resolution wind vector retrieval from QuikSCAT in the Gulf of Maine," *IEEE Geosci. Remote Sens. Lett.*, vol. 6, no. 3, pp. 413–417, Jul. 2009.
- [19] B. A. Williams and D. G. Long, "Estimation of hurricane winds from SeaWinds at ultra high resolution," *IEEE Trans. Geosci. Remote Sens.*, vol. 46, no. 10, pp. 2924–2935, Oct. 2008.
- [20] F. Saïd and D. G. Long, "Effectiveness of QuikSCAT's ultra high resolution images in determining tropical storm eye location," in *Proc. Int. Geosci. Remote Sens. Symp.*, Boston, MA, USA, 21–25, Jul. 2008, vol. 1, pp. 351–354.
- [21] W. T. Liu, K. B. Katsaros, and J. A. Businger, "Bulk parameterization of air–sea exchanges of heat and water vapor including the molecular constraints at the interface," *J. Atmos. Sci.*, vol. 36, no. 9, pp. 1722–1735, Sep. 1979.
- [22] A. B. Kara, A. J. Wallcraft, and M. A. Bourassa, "Air–sea stability effects on the 10 m winds over the global ocean: Evaluations of air–sea flux algorithms," *J. Geophys. Res.*, vol. 113, no. C4, 2008, Art. no. C04009.
- [23] A. Verhoef and A. Stoffelen, "Validation of ASCAT 12.5-km Winds," KNMI, De Bilt, The Netherlands, Tech. Rep., Feb. 2009. [Online]. Available: ftp://podaac.jpl.nasa.gov/allData/ascats/preview/L2/docs/ASCAT_validation_125.pdf
- [24] F. M. Monaldo, D. R. Thompson, R. C. Beal, W. G. Pichel, and P. Clemente-Colón, "Comparison of SAR-derived wind speed with model predictions and ocean buoy measurements," *IEEE Trans. Geosci. Remote Sens.*, vol. 39, no. 12, pp. 2587–2600, Dec. 2001.
- [25] F. M. Monaldo, D. R. Thompson, W. G. Pichel, and P. Clemente-Colón, "A systematic comparison of QuikSCAT and SAR ocean surface wind speeds," *IEEE Trans. Geosci. Remote Sens.*, vol. 42, no. 2, pp. 283–291, Feb. 2004.
- [26] "NOAA STAR Alaska SAR Demonstration Website," NOAA Center Satellite Appl. Res. (STAR), Camp Springs, MD, USA, Dec. 2006, Accessed: 18, Jul. 2014. [Online]. Available: <http://www.star.nesdis.noaa.gov/sod/mecb/sar/index.html>
- [27] C. Nie and D. G. Long, "A C-band scatterometer simultaneous wind/rain retrieval method," *IEEE Trans. Geosci. Remote Sens.*, vol. 46, no. 11, pp. 3618–3631, Nov. 2008.
- [28] M. P. Owen and D. G. Long, "Towards an improved wind and rain backscatter model for ASCAT," in *Proc. IEEE Int. Geosci. Remote Sens. Symp.*, Honolulu, HI, USA, 2010, pp. 2531–2534.
- [29] A. E. Gonzales and D. G. Long, "An assessment of NSCAT ambiguity removal," *J. Geophys. Res.*, vol. 104, no. C5, pp. 11 449–11 457, May 1999.



Richard D. Lindsley (S'08–M'16) received the Ph.D. degree in electrical engineering from Brigham Young University (BYU), Provo, UT, USA, in 2015. From 2008 to 2015, he was with the Microwave Earth Remote Sensing Laboratory, BYU. He is currently with Remote Sensing Systems, Santa Rosa, CA, USA. His research interests include microwave remote sensing and signal processing.



Jeffrey R. Blodgett received the M.S. degree in electrical engineering from Brigham Young University (BYU), Provo, UT, USA, in 2014. From 2012 to 2014, he was a Research Assistant with the Microwave Earth Remote Sensing Laboratory, BYU. He is currently a Systems Engineer with Lockheed Martin Mission Systems and Training, Manassas, VA, USA. His research interests include microwave remote sensing, radar, signal processing, and sonar.



David G. Long (S'80–SM'98–F'08) received the Ph.D. degree in electrical engineering from the University of Southern California, Los Angeles, CA, USA, in 1989. From 1983 to 1990, he was with NASA's Jet Propulsion Laboratory (JPL), Pasadena, CA, where he developed advanced radar remote sensing systems. While at JPL, he was the Project Engineer on the NASA Scatterometer (NSCAT) project, which flew from 1996 to 1997. He also managed the SCANSAT project, the precursor to SeaWinds, which was flown in 1999 on QuikSCAT, in 2002 on ADEOS-II, and in 2014 on the International Space Station. He is currently a Professor with the Department of Electrical and Computer Engineering, Brigham Young University (BYU), Provo, UT, USA, where he teaches upper-division and graduate courses in communications, microwave remote sensing, radar, and signal processing and is the Director of the BYU Center for Remote Sensing. He is the Principal Investigator on several NASA-sponsored research projects in remote sensing. He has over 400 publications in various areas, including signal processing, radar scatterometry, and synthetic aperture radar. His research interests include microwave remote sensing, radar theory, space-based sensing, estimation theory, signal processing, and mesoscale atmospheric dynamics.

Dr. Long has received the NASA Certificate of Recognition several times and is an Associate Editor of the IEEE GEOSCIENCE AND REMOTE SENSING LETTERS.